

**This is a self-archived version of an original article. This version may differ from the original in pagination and typographic details.**

**Author(s):** Ojala, Joonas; Pakarinen, Janne; Papadakis, Philippos; Sorri, Juha; Sandzelius, Mikael; Cox, Daniel M.; Auranen, Kalle; Badran, Hussam; Davies, Paul J.; Grahn, Tuomas; Greenlees, Paul T.; Henderson, Jack; Herzáň, Andrej; Herzberg, Rolf-Dietmar; Hilton, Joshua; Jakobsson, Ulrika; Jenkins, David G.; Joss, David T.; Julin, Rauno; Juutinen, Sakari; Kibédi, Tibor; Konki, Joonas; Lane, Gregory J.; Leino,

**Title:** Reassigning the shapes of the  $0^+$  states in the  $^{186}\text{Pb}$  nucleus

**Year:** 2022

**Version:** Published version

**Copyright:** © The Author(s) 2022















**Rights:** CC BY 4.0

**Rights url:** <https://creativecommons.org/licenses/by/4.0/>

**Please cite the original version:**

Ojala, J., Pakarinen, J., Papadakis, P., Sorri, J., Sandzelius, M., Cox, D. M., Auranen, K., Badran, H., Davies, P. J., Grahn, T., Greenlees, P. T., Henderson, J., Herzáň, A., Herzberg, R.-D., Hilton, J., Jakobsson, U., Jenkins, D. G., Joss, D. T., Julin, R., . . . Wadsworth, R. (2022). Reassigning the shapes of the  $0^+$  states in the  $^{186}\text{Pb}$  nucleus. *Communications physics*, 5, Article 213.  
<https://doi.org/10.1038/s42005-022-00990-4>

## Reassigning the shapes of the $0^+$ states in the $^{186}\text{Pb}$ nucleus

Joonas Ojala <sup>1</sup>, Janne Pakarinen <sup>1✉</sup>, Philippos Papadakis <sup>1,6</sup>, Juha Sorri<sup>1,7</sup>, Mikael Sandzelius<sup>1</sup>, Daniel M. Cox<sup>1,2,8</sup>, Kalle Auranen <sup>1</sup>, Hussam Badran<sup>1</sup>, Paul J. Davies<sup>3</sup>, Tuomas Grahn <sup>1</sup>, Paul T. Greenlees<sup>1</sup>, Jack Henderson <sup>3,9</sup>, Andrej Herzáň <sup>1,4</sup>, Rolf-Dietmar Herzberg<sup>2</sup>, Joshua Hilton<sup>1,2</sup>, Ulrika Jakobsson<sup>1</sup>, David G. Jenkins<sup>3</sup>, David T. Joss<sup>2</sup>, Rauno Julin<sup>1</sup>, Sakari Juutinen<sup>1</sup>, Tibor Kibédi <sup>5</sup>, Joonas Konki<sup>1</sup>, Gregory J. Lane <sup>5</sup>, Matti Leino<sup>1</sup>, Jarkko Liimatainen<sup>1</sup>, Christopher G. McPeake<sup>1,2</sup>, Olavi Neuvonen<sup>1,7</sup>, Robert D. Page<sup>2</sup>, Edward Parr <sup>2</sup>, Jari Partanen<sup>1,10</sup>, Pauli Peura <sup>1</sup>, Panu Rahkila <sup>1</sup>, John Revill<sup>2</sup>, Panu Ruotsalainen<sup>1</sup>, Jan Sarén <sup>1</sup>, Catherine Scholey<sup>1</sup>, Sanna Stolze<sup>1</sup>, Juha Uusitalo<sup>1</sup>, Andrew Ward<sup>2</sup> & Robert Wadsworth <sup>3</sup>

Across the physics disciplines, the  $^{186}\text{Pb}$  nucleus is the only known system, where the two first excited states, together with the ground state, form a triplet of zero-spin states assigned with prolate, oblate and spherical shapes. Here we report on a precision measurement where the properties of collective transitions in  $^{186}\text{Pb}$  were determined in a simultaneous in-beam  $\gamma$ -ray and electron spectroscopy experiment employing the recoil-decay tagging technique. The feeding of the  $0_2^+$  state and the interband  $2_2^+ \rightarrow 2_1^+$  transition have been observed. We also present direct measurement of the energies of the electric monopole transitions from the excited  $0^+$  states to the  $0^+$  ground state. In contrast to the earlier understanding, the obtained reduced transition probability  $B(E2; 2_1^+ \rightarrow 0_2^+)$  value of  $190(80)$  W.u., the transitional quadrupole moment  $|Q_\gamma(2_1^+ \rightarrow 0_2^+)| = 7.7(33)$  eb and intensity balance arguments provide evidence to reassign the  $0_2^+$  and  $0_3^+$  states with predominantly prolate and oblate shape, respectively. Our work demonstrates a step-up in experimental sensitivity and paves the way for systematic studies of electric monopole transitions in this region. These electric monopole transitions probe the nuclear volume in a unique manner and provide unexploited input for development of the next-generation energy density functional models.

<sup>1</sup> Accelerator Laboratory, Department of Physics, University of Jyväskylä, FI-40014 Jyväskylä, Finland. <sup>2</sup> Department of Physics, Oliver Lodge Laboratory, University of Liverpool, P.O. Box 147, Liverpool L69 7ZE, UK. <sup>3</sup> Department of Physics, University of York, York YO10 5DD, UK. <sup>4</sup> Institute of Physics, Slovak Academy of Sciences, SK-84511 Bratislava, Slovakia. <sup>5</sup> Department of Nuclear Physics and Accelerator Applications, Research School of Physics, The Australian National University, Canberra, ACT 2601, Australia. <sup>6</sup> Present address: STFC Daresbury Laboratory, Daresbury, Warrington WA4 4AD, UK. <sup>7</sup> Present address: Radiation and Nuclear Safety Authority - STUK, Jokiniemenkuja 1, 01370 Vantaa, Finland. <sup>8</sup> Present address: Department of Physics, Lund University, SE-22100 Lund, Sweden. <sup>9</sup> Present address: Department of Physics, University of Surrey, Guildford GU2 7XH, UK. <sup>10</sup> Deceased: Jari Partanen. ✉email: [janne.pakarinen@jyu.fi](mailto:janne.pakarinen@jyu.fi)

The governing interactions in atomic nuclei give rise to diverse quantum phenomena such as single-particle motion, nucleon pairing and collectivity, and can result in a configuration that prefers a specific shape. At one extreme, competing shape-driving configurations can appear within a small energy range, a phenomenon commonly known as shape coexistence.

One of the richest regions of shape coexistence is formed by very neutron-deficient nuclei with proton number  $Z$  close to the magic number 82 and neutron number  $N$  close to 104 (mid-shell)<sup>1,2</sup>. Shape coexistence in this region was first established in the early 1970s in laser spectroscopy experiments that discovered a sudden change in the nuclear charge distribution of neutron-deficient Hg isotopes<sup>3</sup>. Over the years, a whole arsenal of spectroscopic techniques has been employed to study the competing structures in this region. For example, rotational bands have been investigated via in-beam  $\gamma$ -ray spectroscopy<sup>4</sup>,  $\beta$ -decay and  $\alpha$ -decay fine structure measurements have probed the level energies of the band-head  $0^+$  states<sup>5–7</sup>, whereas lifetime and Coulomb excitation experiments have shed light on the collectivity of transitions connecting the low-spin states<sup>8–11</sup>. The lifetimes of excited  $0^+$  states have been measured for <sup>190,192,194</sup>Pb nuclei<sup>12</sup>.

The discovery of two low-lying excited  $0^+$  states in the  $N = 104$  neutron mid-shell nucleus <sup>186</sup>Pb in an  $\alpha$ -decay fine-structure experiment established a feature in the atomic nucleus that remains unique across different physics domains<sup>5</sup>. While in its ground state the <sup>186</sup>Pb nucleus is spherical<sup>13</sup>, its first and second excited states were associated with predominantly  $\pi(2p - 2h)$  and  $\pi(4p - 4h)$  excitations across the  $Z = 82$  shell gap and assigned with deformed oblate and prolate shape, respectively<sup>5</sup>. This triplet of  $0^+$  states, which lie within an excitation energy range of 700 keV, represents a system where the perturbation of the ground state by less than half a per mille of its binding energy results in configuration changes that are associated with different shapes. However, despite all efforts, the linking transitions from rotational bands to the deformed band-head  $0^+$  states have remained unobserved. Results from previous in-beam spectroscopy experiments on <sup>186</sup>Pb have been reported in refs. 14–18. In contrast to ref. 5, many theoretical works<sup>18–29</sup> have proposed opposite shape assignments for the  $0^+$  states. The band-head  $0^+$  states are the lowest excited states, which due to angular momentum conservation, can only de-excite via electric monopole ( $E0$ ) transitions. Therefore, in-beam observation of conversion electrons is required.

In the present work, results from an in-beam spectroscopic study of <sup>186</sup>Pb employing the SAGE spectrometer<sup>30</sup> are presented. SAGE is a state-of-the-art instrument that builds on years of endeavour put into research and development of  $\gamma$ -ray<sup>31</sup> and solenoidal electron<sup>32,33</sup> spectrometers. It allowed for the needed gain in sensitivity to probe the transitions between the low-spin states in <sup>186</sup>Pb and provided the first rigorous experimental evidence that supports the assignment of the  $0_2^+$  state with predominantly prolate shape. The present work responds to an increasing demand, also recalled in the recent review article<sup>34</sup>, to advance our understanding on electric monopole transitions.

## Results

Recoil-gated,  $\alpha$ -tagged (RDT from now on) background subtracted prompt  $\gamma$ -ray and conversion-electron energy spectra are shown in Figs. 1 and 2, respectively. The most prominent  $\gamma$ -ray peaks have been labelled according to their transition energies. The region covering the non-yrast band, which is associated with an oblate shape, is expanded in the inset of Fig. 1. In the electron-energy spectrum in Fig. 2, the most prominent conversion-electron lines with corresponding K-, L- and M-components have

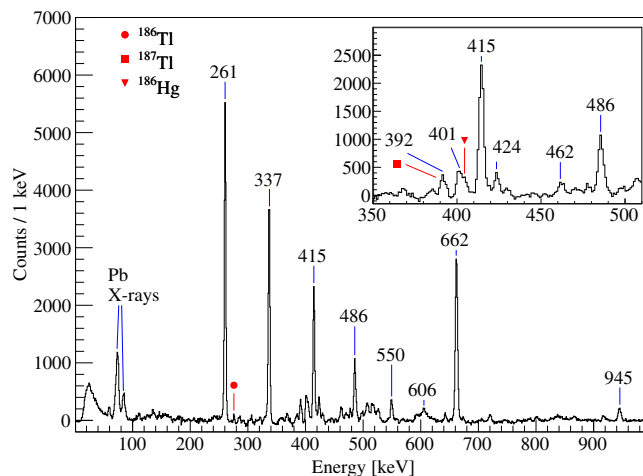


**Fig. 1 Recoil-gated,  $\alpha$ -tagged background-subtracted  $\gamma$ -ray energy spectrum.** The most prominent peaks are marked with transition energies. The inset shows a close-up of the energy region from 350 to 510 keV. The contaminant transitions and their parent nuclei are marked with the red symbols.

been marked and labelled accordingly. The low-energy region below 150 keV is dominated by the  $\delta$ -electron background.

Deconvolution of the electron energy spectrum has been performed and overlaid in Fig. 2. The blue line illustrates the total fit made for the electron energy spectrum. The dotted lines correspond to the calculated K-, L- and M-electron components of the most prominent  $E2$  and  $M1$  transitions, also including contaminant events. After subtracting the calculated components from the total fit, there remains an excess of electron counts, indicated by the red line in Fig. 2. This excess will be discussed below.

The high-statistics RDT  $\gamma - \gamma$  and  $\gamma - e^-$  coincidence data allowed new transitions in <sup>186</sup>Pb to be established. The properties of the new transitions and transitions relevant to the present work are listed in Table 1. Based on coincidence relations and intensity balances, the new transitions have been placed in the level scheme as shown in Fig. 3. It is interesting to note that, despite the same target and beam combination as in refs. 17,18, the slightly higher beam energy of the present work resulted in much higher relative feeding of the non-yrast states in <sup>186</sup>Pb.

**De-excitation path passing through the  $0_2^+$  state.** An electron peak at 447 keV stands out in the RDT electron-energy spectrum, see Fig. 2. The peak cannot be associated with any previously known  $\gamma$ -ray transition in <sup>186</sup>Pb, suggesting the transition has a strong  $E0$  component. If this is considered to be a K-conversion electron component, the corresponding transition energy would be 535 keV and the L-conversion electron component would have an energy of 520 keV. Indeed, an electron peak at that energy is observed in the RDT electron energy spectrum in Fig. 2. These are in a perfect agreement with the  $0_2^+ \rightarrow 0_1^+$  transition energy extracted in the  $\alpha$ -decay of <sup>190</sup>Po<sup>5</sup>, confirming the earlier discovery of the  $0_2^+$  state and the assignment of electron peaks in Fig. 2 with a transition energy of 535 keV.

The de-excitation path passing through the  $0_2^+$  state at 535 keV is investigated in Fig. 4. An RDT  $\gamma$ -ray energy spectrum in coincidence with the 447 keV prompt electrons is presented in Fig. 4a. In addition to the known yrast-band transitions, a peak at 125.0(24) keV is observed. The energy matches with the level energy difference of 127(2) keV between the  $2_1^+$  and  $0_2^+$  states, thus the transition has been placed in the level scheme accordingly. The groups of counts appearing at around 160 and 350 keV could not

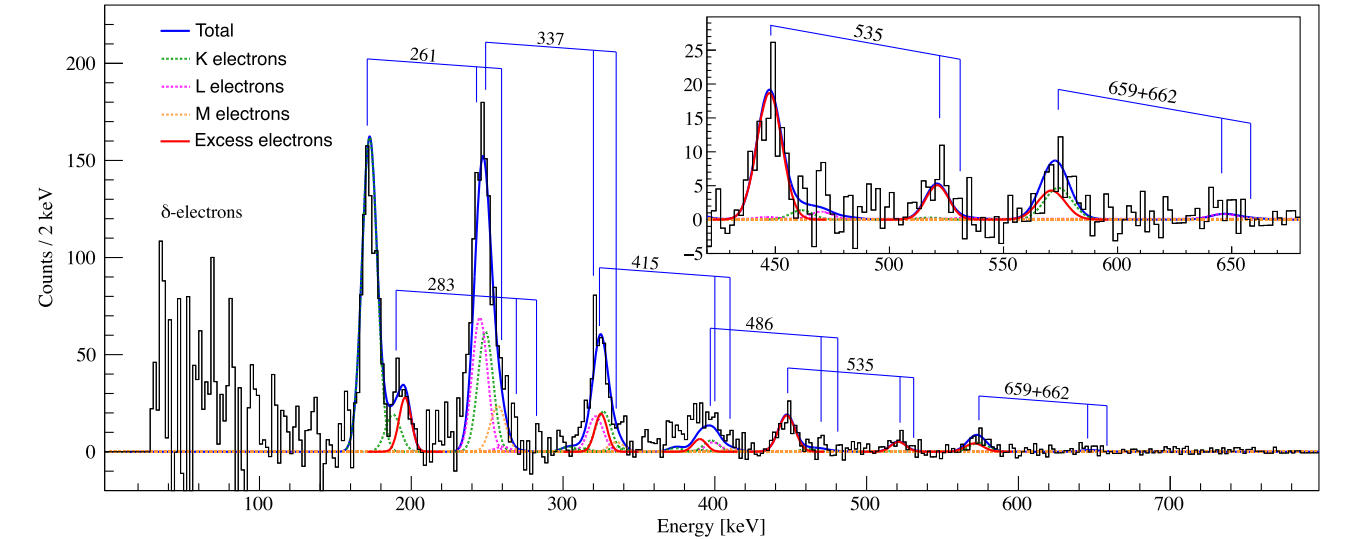


**Fig. 2 Recoil-gated,  $\alpha$ -tagged background-subtracted electron energy spectrum.** The K-, L- and M-components of the most prominent transitions are marked and labelled with transition energies. The total fit is shown with the blue line. The green, purple and orange dotted lines indicate the calculated K-, L- and M-electron components extracted from the corresponding  $\gamma$ -ray intensities, respectively. The excess electrons are marked with the red line. The  $\delta$ -electron flux dominates below 150 keV. The inset shows a close-up of high-energy transitions.

Table 1 Transition properties obtained in the present work.						
$J_i^\pi \rightarrow J_f^\pi$	$E_{J_i^\pi \rightarrow J_f^\pi}$	$I_\gamma$	$E_K$	$I_K$	$E_L$	$I_L$
Yrast-band transitions						
$2_1^+ \rightarrow 0_2^+$	127(2) <sup>a</sup>	9(3) <sup>b</sup>	39(1)	4(2) <sup>b</sup>	113(1)	13(4) <sup>b</sup>
$4_1^+ \rightarrow 2_1^+$	260.6(2)	790(30)	173(1)	60(13)	244(3)	50(15)
$6_1^+ \rightarrow 4_1^+$	337.0(2)	680(22)	248(2)	43(12)		
$8_1^+ \rightarrow 6_1^+$	414.6(2)	445(31)				
$10_1^+ \rightarrow 8_1^+$	485.8(2)	255(9)				
$12_1^+ \rightarrow 10_1^+$	549.6(2)	103(6)				
$14_1^+ \rightarrow 12_1^+$	605.6(4)	34(9)				
Non-yrast band transitions						
$4_2^+ \rightarrow 2_2^+$	391.9(2)	71(17)				
$6_2^+ \rightarrow 4_2^+$	401.0(2)	66(17)				
$8_2^+ \rightarrow 6_2^+$	423.8(2)	61(18)				
$(10_2^+) \rightarrow 8_2^+$	462.2(2)	66(11)				
Interband transitions						
$0_2^+ \rightarrow 0_1^+$	535(2)		447(2)	22(5)	522(2)	8(6)
$0_3^+ \rightarrow 0_1^+$	659(4)		571(4)	11(7) <sup>c</sup>		
$2_1^+ \rightarrow 0_1^+$	662.1(2)	1000				
$2_2^+ \rightarrow 0_1^+$	945.1(2)	115(4)				
$2_2^+ \rightarrow 2_1^+$	283.0(3) <sup>a</sup>	<20 <sup>d</sup>	196(2) <sup>e</sup>	10(5) <sup>e</sup>		
$4_2^+ \rightarrow 4_1^+$	413.9(4) <sup>f</sup>	38(28) <sup>f</sup>	324(2) <sup>c</sup>	12(8) <sup>c</sup>		
$6_2^+ \rightarrow 6_1^+$	479.0(3) <sup>g</sup>	27(22) <sup>g</sup>				
Spins and parities of the initial and final states ( $J_i^\pi$ and $J_f^\pi$ ) are given in the first column. Transition energies ( $E_{J_i^\pi \rightarrow J_f^\pi}$ ), $\gamma$ -ray intensities ( $I_\gamma$ ) and K- and L-conversion electron energies ( $E_K$ , $E_L$ ) and intensities ( $I_K$ and $I_L$ ) are listed in the other columns. Unless otherwise noted, the intensities are extracted from the recoil-gated, $\alpha$ -tagged $\gamma$ -ray or electron singles energy spectra. Energies are given in the units of keV and intensities are normalized to the $\gamma$ -ray intensity of the $2_1^+ \rightarrow 0_1^+$ transition.						
<sup>a</sup> Extracted from level energy difference.						
<sup>b</sup> From recoil-gated, $\alpha$ -tagged $0_2^+ \rightarrow 0_1^+$ K electrons with a gate on the $4_1^+ \rightarrow 2_1^+$ $\gamma$ -ray transition.						
<sup>c</sup> Value and uncertainty extracted from the deconvolution of the corresponding electron peak.						
<sup>d</sup> From recoil-gated, $\alpha$ -tagged $\gamma$ rays in coincidence with the $2_1^+ \rightarrow 0_1^+$ $\gamma$ -ray transition.						
<sup>e</sup> Weighted average, see text for more details.						
<sup>f</sup> From $\gamma$ - $\gamma$ coincidence data.						
<sup>g</sup> From recoil-gated, $\alpha$ -tagged $\gamma$ -ray energy spectrum with a gate on 424 keV $\gamma$ rays.						

be assigned with any transitions in  $^{186}\text{Pb}$ . The total intensity value of  $I_{\text{total}}(2_1^+ \rightarrow 0_2^+) = 31(10)$  was extracted from the weighted average of the  $0_2^+ \rightarrow 0_1^+$  K-electron events normalised with the K-electron components of the  $2_1^+ \rightarrow 0_1^+$ ,  $6_1^+ \rightarrow 4_1^+$  and  $8_1^+ \rightarrow 6_1^+$  transitions observed in coincidence with the  $4_1^+ \rightarrow 2_1^+$   $\gamma$ -ray transition. The corresponding spectrum is shown in Fig. 4b, where the presence of the K-conversion electrons of the 535 keV transition and peaks used for normalisation are evident. The spectrum also includes events at  $\sim 113$  keV that could correspond to the L-conversion electrons originating from the  $2_1^+ \rightarrow 0_2^+$  transition as expected from the high L-conversion coefficient of  $\alpha_L \approx 1.4$ . However, they overlap with the  $\delta$ -electron background preventing precise extraction of the energy and intensity. The  $\gamma$ -ray intensity value of  $I_\gamma(2_1^+ \rightarrow 0_2^+) = 9(3)$  was obtained using the

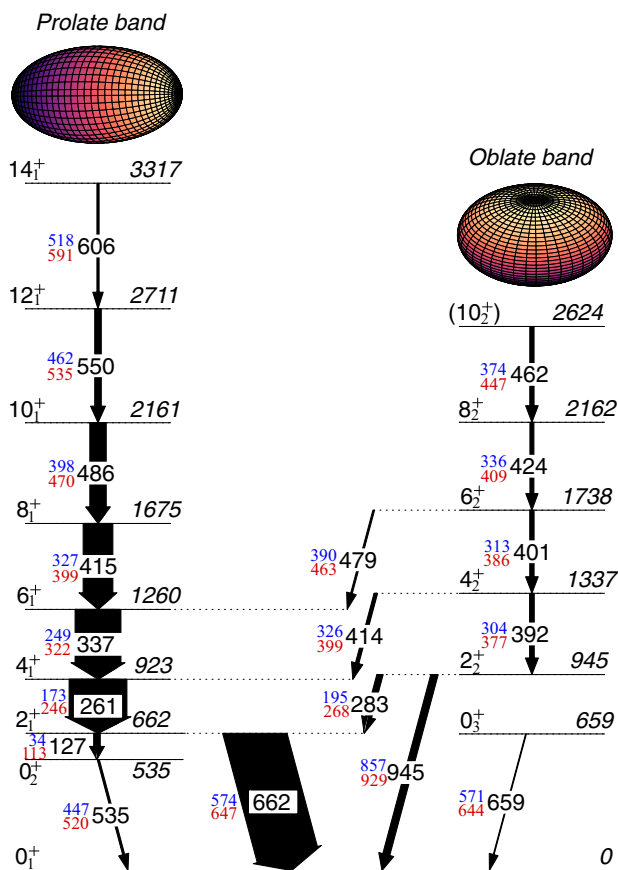


**Fig. 3** Partial level scheme of  $^{186}\text{Pb}$  presenting transitions relevant to the present work. The widths of the arrows are proportional to the total transition intensities. The K- and L-conversion electron energies have been labelled in blue and red, respectively.

value  $\alpha_{\text{total}}(E2) = 2.35(4)^{35}$ . Such a small intensity is beyond the observational limit in the RDT  $\gamma$ -ray singles events.

**Observation of the  $E0$  transition de-exciting the  $0_3^+$  state.** A group of events is found in the RDT electron-energy spectrum around 574 keV (Fig. 2) where the K-conversion electron component of the  $E2(2_1^+ \rightarrow 0_1^+)$  transition is expected. Based on the observed  $\gamma$ -ray intensity and the calculated K-conversion coefficient<sup>35</sup>, the number of corresponding K-conversion events in the peak has been determined. As a result, the intensity of the peak at  $\sim 574$  keV cannot be solely explained by the  $2_1^+ \rightarrow 0_1^+$  transition or by other observed  $\gamma$ -ray transitions. It is also noteworthy, that the full width at half maximum resolution of the peak is 17 keV, which is larger than the expected resolution of  $\sim 14$  keV. Thus, it is considered the peak comprises two components, one that is assigned with the  $2_1^+ \rightarrow 0_1^+$  transition and the other to the excess events. The composition of the peak with the corresponding fits is visualised in Fig. 5. The centroid of the excess events is at 571 keV. If this was an L-conversion electron component of a transition, the corresponding more intense K-component should be observed at 498 keV, which is clearly not the case. The non-observation of a corresponding  $\gamma$ -ray transition suggests a strong  $E0$  component. The suggested energy of 659(4) keV is in excellent agreement with the  $0_3^+ \rightarrow 0_1^+$  transition [650(20) keV] first observed in the  $\alpha$ -decay of  $^{190}\text{Po}$ <sup>5</sup>. Consequently, the 571 keV electron peak is assigned as the K-conversion electron component of the  $0_3^+ \rightarrow 0_1^+$  transition

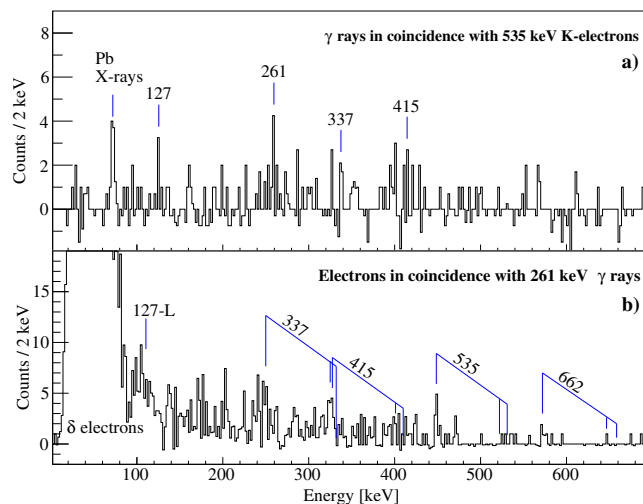


**Fig. 4** Evidence for the de-excitation path passing through the  $0_2^+$  state.

**a** Recoil-gated,  $\alpha$ -tagged background subtracted  $\gamma$ -ray energy spectrum with a gate on the K-electrons of the 535 keV transition. **b** Recoil-gated,  $\alpha$ -tagged background subtracted electron energy spectrum with a gate on the 261 keV  $\gamma$  rays. The peaks associated with  $^{186}\text{Pb}$  have been labelled with corresponding transition energies and positions of the K-, L- and M-conversion components are marked. The position of the L-electron component of the  $2_1^+ \rightarrow 0_2^+$  transition (113 keV) is marked for visualisation.

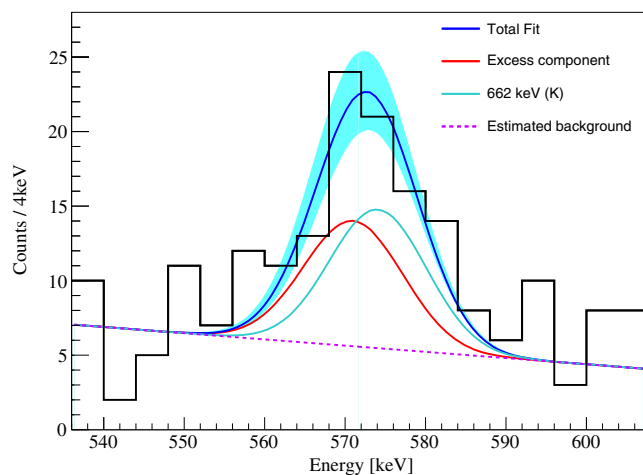


**Fig. 5** Close-up of the recoil-gated,  $\alpha$ -tagged electron energy spectrum around 570 keV.

The total fit (blue) includes two components, one is associated with the  $2_1^+ \rightarrow 0_1^+$  transition (cyan) and the other with the  $0_3^+ \rightarrow 0_1^+$  transition (red). The uncertainty of the total fit at the  $1\sigma$  level is shown with light blue band. The purple dashed line illustrates the extracted background.

with  $I_K(0_3^+ \rightarrow 0_1^+) = 11(7)$ . Unfortunately, transitions feeding the  $0_3^+$  state are beyond the observational limit.

**Discovery of the interband  $2_2^+ \rightarrow 2_1^+$  transition.** The interband  $2_2^+ \rightarrow 2_1^+$  transition has not been observed previously. The missing  $\gamma$ -ray intensity analysis based on  $\gamma$ - $\gamma$  coincidences, similar to that performed for  $^{188}\text{Pb}$  which revealed considerable  $E0$  components in the interband  $J \rightarrow J$  transitions<sup>36</sup>, did not indicate any strong  $E0$  components in  $^{186}\text{Pb}$ <sup>17,18</sup>. However, this could be explained by insufficient  $\gamma$ - $\gamma$  statistics as the intensity balances listed in Table 1 of ref. 18 do not rule out an additional transition feeding the  $2_1^+$  state.



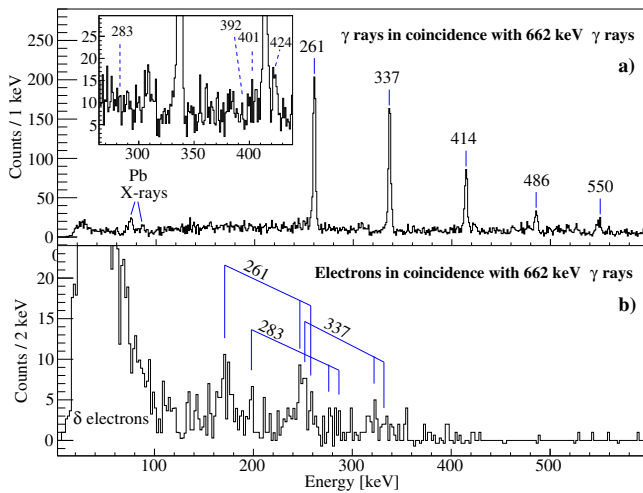


**Fig. 6 Evidence for the highly-converted  $2_2^+ \rightarrow 2_1^+$  transition.** Recoil-gated,  $\alpha$ -tagged  $\gamma$ -ray (a) and electron (b) energy spectra in coincidence with 662 keV  $\gamma$  rays. The most prominent peaks have been labelled with corresponding transition energies and positions of the K-, L- and M-conversion components are marked.

The present RDT electron data show evidence for the K-conversion electron component of a  $2_2^+ \rightarrow 2_1^+$  283 keV transition as demonstrated in the RDT electron energy spectrum in Fig. 2. The electron peak overlaps partly with the K-conversion electron component of the contaminant  $(11^-) \rightarrow (10^-)$  276 keV transition in  $^{186}\text{Tl}$ . Based on the recoil-gated  $\gamma$ - $\gamma$  and  $\gamma$ - $e^-$  coincidence data, a value of  $\alpha_{K,\text{exp}}(276) = 0.33(7)$  was obtained. This is in-line with the calculated value of  $\alpha_{K,M1}(276) = 0.404(6)$  for an M1 transition<sup>35</sup>. Accordingly, the K-conversion electron component of the contaminant 276 keV M1 transition is plotted (green dashed line) in Fig. 2. The total fit (blue line) shows the sum of the excess electrons in  $^{186}\text{Pb}$  (red line) and the M1 transition in  $^{186}\text{Tl}$  and matches well with the observed electrons.

Further evidence for the highly-converted  $2_2^+ \rightarrow 2_1^+$  transition is presented in Fig. 6, where RDT  $\gamma$ -ray (a) and electron (b) energy spectra in coincidence with 662 keV  $\gamma$  rays stemming for the  $2_1^+ \rightarrow 0_1^+$  transition are shown. The  $\gamma$ -ray energy spectrum in Fig. 6a presents peaks associated with yrast-band transitions, whereas the  $\gamma$ -ray transition at 283 keV (see the inset) is absent. The upper limit for the  $\gamma$ -ray intensity of the  $2_2^+ \rightarrow 2_1^+$  transition was estimated to be  $I_\gamma < 20$ . It is noteworthy, that apart from the  $8_2^+ \rightarrow 6_2^+$  transition at 424 keV with  $I_\gamma = 61(18)$ , other non-yrast transitions are below the observational limit in Fig. 6a. In Fig. 6b, in addition to the two preceding yrast-band transitions, an electron peak emerges at 196(2) keV corresponding to the energy of the K-conversion electron component of the 283 keV  $2_2^+ \rightarrow 2_1^+$  transition. The intensity of the K-conversion electron component  $I_K(2_2^+ \rightarrow 2_1^+) = 10(5)$  given in Table 1 is the weighted average of intensities extracted from RDT singles electrons (Fig. 2) and from RDT electrons with a gate on the  $2_1^+ \rightarrow 0_1^+$   $\gamma$ -ray transition (Fig. 6). Based on obtained intensities, the lower limit of  $\alpha_K > 0.5$  for the conversion coefficient can be extracted.

#### Electron-conversion component of the $4_2^+ \rightarrow 4_1^+$ transition.

The  $\gamma$ - $e^-$  coincidence statistics were not sufficient to obtain information about the conversion-electron component of the interband  $4_2^+ \rightarrow 4_1^+$  transition by gating on the feeding transition. Since the  $4_2^+ \rightarrow 4_1^+$  transition energy overlaps with the  $8_1^+ \rightarrow 6_1^+$  transition energy, gating with a transition below the  $4_1^+$  state included both transitions and resulted in too few statistics for deconvolution analysis. However, RDT  $\gamma$ -ray and electron singles

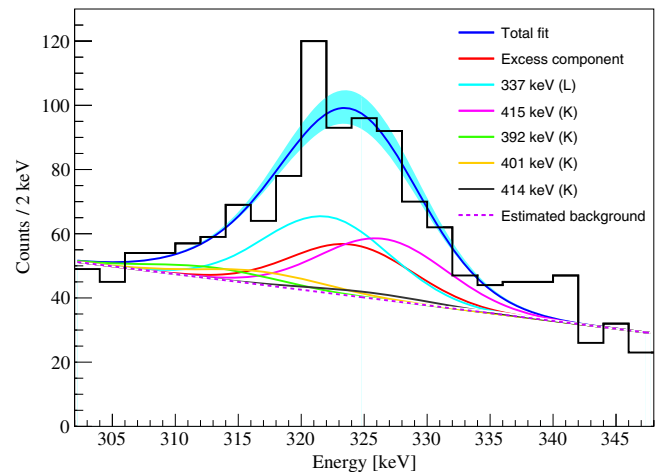


**Fig. 7 Close-up of the recoil-gated,  $\alpha$ -tagged electron energy spectrum around 325 keV.** The total fit (blue) consists of components determined from the measured  $\gamma$ -ray intensities and the excess electrons are associated with the  $4_2^+ \rightarrow 4_1^+$  transition. Components extracted from the observed  $\gamma$  rays are labelled according to transition energies and electron shells of origin. The uncertainty of the total fit at the  $1\sigma$  level is shown with a light blue band and the purple dashed line illustrates the extracted background.

data were sufficient for the deconvolution of the electron energy spectrum based on the extracted  $\gamma$ -ray intensities. This is illustrated in Fig. 7, where a peak at the corresponding K-conversion electron energy has been divided into its components. The properties of these five components, as identified in Fig. 7, are based on the observed E2  $\gamma$ -ray transitions. A comparison of the sum of the calculated intensities of the electron components to the measured electron energy spectrum reveals a clear excess of electrons. In order to match with the experimental observations, an additional electron excess component (red line in Fig. 7) with free fit parameters has been included, leading to a measured intensity of  $I = 12(8)$ . If the electron excess was of L-electron origin, the corresponding K-electron line at 252 keV should be observed, which is not the case. An  $\alpha_K = 0.32(30)$  conversion coefficient was extracted for the  $4_2^+ \rightarrow 4_1^+$  transition.

#### Discussion

The  $\alpha_K > 0.5$  value obtained for the  $2_2^+ \rightarrow 2_1^+$  transition is higher than expected for an M1, E2 or mixed E2/M1 transition ( $\alpha_{K,M1} = 0.409$ ,  $\alpha_{K,E2} = 0.075$ ), suggesting the presence of an E0 component. This is only possible for a  $\Delta K = 0$  transition between states having the same spin and parity. Consequently, the level at 945 keV can be firmly assigned as the  $J_i^\pi = 2_2^+$  state. Using similar arguments for the  $4_2^+ \rightarrow 4_1^+$  transition, the tentative assignment of the  $(4_2^+)$  state at 1337 keV in refs. 17,18 can be now fixed. Based on these assignments and the angular distribution information in refs. 17,18, levels at 1738 and 2162 keV can be also firmly assigned as  $J_i^\pi = 6_2^+$  and  $J_i^\pi = 8_2^+$  states, respectively. Accordingly, spins and parities of the non-yrast band up to the  $8_2^+$  state are fixed. It also follows from the  $\Delta K = 0$  criteria that the M1 components for the interband transitions are ruled out.

The E0 transition probability is defined as

$$W(E0) = \rho^2 \times \Omega(E0), \quad (1)$$

where  $\rho^2$  is the transition monopole strength and  $\Omega(E0)$  is the electronic factor<sup>37,38</sup>. For the monopole strength, the following relation can be extracted:

$$\rho^2 = \frac{I_K(E0) W_\gamma(E2)}{I_\gamma(E2) \Omega_K(E0)}, \quad (2)$$

where  $I_K(E0)$  is the K-conversion electron intensity of the  $E0$  transition,  $I_\gamma(E2)$  and  $W_\gamma(E2)$  are the  $\gamma$ -ray intensity and transition rate of the competing  $E2$  transition, respectively, and  $\Omega_K(E0)$  is the electronic factor for the K-electron conversion of the  $E0$  transition.

Although the information on the transition rates is lacking, it is intriguing to use estimates to evaluate the monopole strengths of the interband transitions. A  $B(E2; 2_1^+ \rightarrow 0_1^+) = 6$  W.u. has been extracted from the lifetime of the  $2_1^+$  state<sup>8,9</sup>, while  $B(E2; 2_2^+ \rightarrow 0_1^+) = 3.9$  W.u. has been measured for  $^{184}\text{Hg}$  in a Coulomb excitation experiment<sup>10</sup>. In both cases, transitions are between states of different intrinsic configurations. Assuming  $B(E2; 2_2^+ \rightarrow 0_1^+) = 5$  W.u., a  $\rho^2$  monopole strength value of  $100(60) \times 10^{-3}$  can be extracted for the  $E0$  component of the  $2_2^+ \rightarrow 2_1^+$  transition. Similarly,  $\rho^2 = 40(30) \times 10^{-3}$  can be obtained from the present data for the  $4_2^+ \rightarrow 4_1^+$  transition assuming  $B(E2; 4_2^+ \rightarrow 2_2^+) = 100$  W.u., a typical value for an oblate band<sup>8,9</sup>.

A large monopole strength is a fingerprint of mixing between two coexisting states with different deformation<sup>39</sup>. Since the spherical  $J^\pi$  states are expected to lie well above the energy of the prolate and oblate  $J^\pi$  states, they can be omitted in the following mixing calculations. According to the two-level mixing model, the monopole strength can be expressed as:

$$\rho^2 = \left(\frac{3}{4\pi}Z\right)^2 a^2 b^2 [\beta_{2,1}^2 - \beta_{2,2}^2]^2, \quad (3)$$

where  $Z$  is the atomic number,  $a$  and  $b$  are the mixing amplitudes with the relation  $a^2 + b^2 = 1$  and  $\beta_{2,i}$  is the quadrupole deformation parameter of the  $J_i^\pi$  state. Quadrupole deformation values of  $|\beta_2| = 0.29(5)$  and  $|\beta_2| = 0.17(3)$  have been extracted for the prolate and oblate bands, respectively, from lifetime measurements performed in this region<sup>8,9</sup>. Adopting these values, the amount of mixing needed to produce the monopole strength estimated for the  $2_2^+ \rightarrow 2_1^+$  transition is of the order of 10% ( $a^2 = 0.9$ ), while it is only  $\sim 4\%$  ( $a^2 = 0.96$ ) for the  $4_2^+ \rightarrow 4_1^+$  transition. It is noteworthy, that the presence of a possible  $M1$  component in the interband transitions would reduce the value obtained for the monopole strength, further decreasing the amount of mixing. Accordingly, small prolate-oblate mixing can be expected for the yrast  $2_1^+$  and  $4_1^+$  states, which is in line with the results obtained in the lifetime measurements<sup>8,9</sup>. Calculations performed in the IBM framework predict more pronounced mixing<sup>40</sup>.

The intra-band transition intensities of the non-yrast band (oblate) were extracted to be around 10% of the corresponding yrast-band (prolate) transitions and with decreasing spin the majority of the de-excitation of the non-yrast states ends up to the yrast band. The feeding of the excited  $0^+$  states is weak as the feeding transitions have to compete against higher energy transitions to the  $0^+$  ground state. In the present work, the first and second excited  $0^+$  states were fed at the level of  $\sim 2.2\%$  and  $\sim 1.1\%$  of the total intensity feeding the ground state, respectively.

The only observed feeding of the  $0_2^+$  state is via the  $2_1^+ \rightarrow 0_2^+$  transition. Based on the branching ratios and the lifetime of the  $2_1^+$  state  $[18(5)\text{ ps}]$ <sup>8,9</sup>, a reduced transition probability  $B(E2; 2_1^+ \rightarrow 0_2^+) = 190(80)$  W.u. can be obtained. For comparison, a weighted average of  $B(E2)$  values measured for higher-spin prolate band transitions in  $^{186,188}\text{Pb}$  nuclei is  $390(40)$  W.u. The transition quadrupole moments  $|Q_i|$  extracted from these  $B(E2)$  values under the assumption of a rotating quadrupole-deformed nucleus are  $7.7(33)$  eb and  $9.0(5)$  eb, respectively, suggesting that the  $0_2^+$  state has a predominant prolate component.

The de-excitation of the  $0_2^+$  state with  $I_{\text{total}}(0_2^+ \rightarrow 0_1^+) = 26(6)$  extracted from the corresponding K-electron peak in the singles RDT electron energy spectrum of Fig. 2 is fully covered by the

feeding transition with the intensity of  $I_{\text{total}}(2_1^+ \rightarrow 0_2^+) = 31(10)$  extracted from the electron energy spectrum of Fig. 4 gated with 261 keV  $\gamma$  rays. Nevertheless, it is interesting to estimate the potential side-feeding within the given margins. As discussed earlier, the  $2_2^+$  state can be considered almost pure oblate state. Provided the  $0_2^+$  state were predominantly oblate, the  $B(E2; 2_2^+ \rightarrow 0_2^+)$  value could be estimated to be  $\sim 50$  W.u. Assuming  $B(E2; 2_2^+ \rightarrow 0_1^+) = 5$  W.u., an intensity value of  $I_{\text{total}}(2_2^+ \rightarrow 0_2^+) = 19(2)$  can be obtained. Such a large side-feeding does not fit within the given margins, suggesting the  $0_2^+$  state does not have a notable oblate admixture.

The  $0_3^+/0_2^+$  mixing can be further assessed using monopole strengths obtained for the transitions from the  $0_3^+$  state. Applying Eq. (3) and typical prolate and oblate quadrupole deformation values of  $|\beta_2| = 0.29(5)$  and  $|\beta_2| = 0.17(3)$ <sup>8,9</sup>, respectively, the value of  $\rho^2(0_3^+ \rightarrow 0_2^+) = 290 \times 10^{-3}$  is obtained for maximal prolate-oblate mixing (i.e.  $a^2 = b^2 = 0.5$ ). Based on the lifetimes of the predominantly oblate  $0_2^+$  states in  $^{190,192,194}\text{Pb}$  nuclei<sup>12</sup>, a  $\rho^2 = 10 \times 10^{-3}$  value is estimated for the  $0_3^+ \rightarrow 0_1^+$  transition. Consequently, by using  $I_{\text{total}}(0_3^+ \rightarrow 0_1^+) = 13(8)$  obtained in the present work,  $I_{\text{total}}(0_3^+ \rightarrow 0_2^+) = 170(100)$  can be extracted. In the case of smaller prolate-oblate mixing (e.g.  $a^2 = 0.05$ ),  $I_{\text{total}}(0_3^+ \rightarrow 0_2^+) = 34(20)$  is obtained. While there is not much room for side-feeding for the  $0_2^+$  state, the small amount of mixing between the excited  $0^+$  states is better in line with the extracted intensity balances.

The feeding of the  $0_3^+$  state was beyond the observational limit. Taking  $B(E2; 2_2^+ \rightarrow 0_1^+) = 5$  W.u. as above and assuming the feeding of the  $0_3^+$  state is solely from a predominantly oblate  $2_2^+$  state, a reduced transition probability of  $B(E2; 2_2^+ \rightarrow 0_3^+) = 200(120)$  W.u. can be obtained. This shows that the  $2_2^+ \rightarrow 0_3^+$  transition can be a collective transition within a band.

To conclude, the  $B(E2)$  value shows that the  $2_1^+ \rightarrow 0_2^+$  transition is a collective transition, whereas the transition quadrupole moment, albeit with large uncertainty, suggests a transition within the prolate band rather than a transition between different configurations. The intensity balances between the low-spin states imply small mixing between the excited  $0^+$  states. In particular, the oblate admixture in the  $0_2^+$  state has been found to be small. Consequently, the  $0_2^+$  state is assigned as the band-head of the yrast band and associated with predominantly prolate shape. Accordingly, the  $0_3^+$  state is considered to be the band-head of the non-yrast band associated with predominantly oblate shape. In Fig. 8, level energy systematics in the neutron-deficient even-mass Pb nuclei has been plotted including the new assignments of the  $0^+$  states. The parabolic behaviour of the intruder states is now more evident at the minima that take place at  $N = 104$  and  $N = 106$  for prolate and oblate configurations, respectively. This is also well in-line with the very recent study on the odd-mass  $^{187}\text{Pb}$  nucleus with  $N = 105$  which shows that the prolate minimum is below the oblate one in energy<sup>41</sup>.

Many theoretical calculations predict the prolate minimum in  $^{186}\text{Pb}$  to be lower in energy than the oblate one (see refs. 18–29), although opposite results have also been obtained<sup>5,42,43</sup>. Moreover, the lowest oblate minimum in energy is predicted at  $N = 106$  by several calculations<sup>20,22,24,26–29</sup> and experimental findings support the oblate assignment of the  $0_2^+$  state in  $^{188}\text{Pb}$ <sup>44</sup>. Based on the IBM calculations for  $^{186}\text{Pb}$ , the  $0_3^+$  [ $0_3^+$ ] state is a mixture of configurations assigned with spherical, prolate and oblate shapes with admixtures of 3% [3%], 63% [38%] and 34% [58%] weights in their wave function, respectively<sup>40</sup>. Experimental results obtained on mixing of the  $0^+$  states are only available for the oblate and spherical states in the heavier  $^{190,192,194}\text{Pb}$  isotopes<sup>45</sup>.

However, the fact that the assignments of the excited  $0^+$  states presented here are in contrast to what was proposed by Andreyev et al. warrants further discussion. Their arguments were based on (i) the level energy systematics of the oblate  $0^+$  states, (ii) the

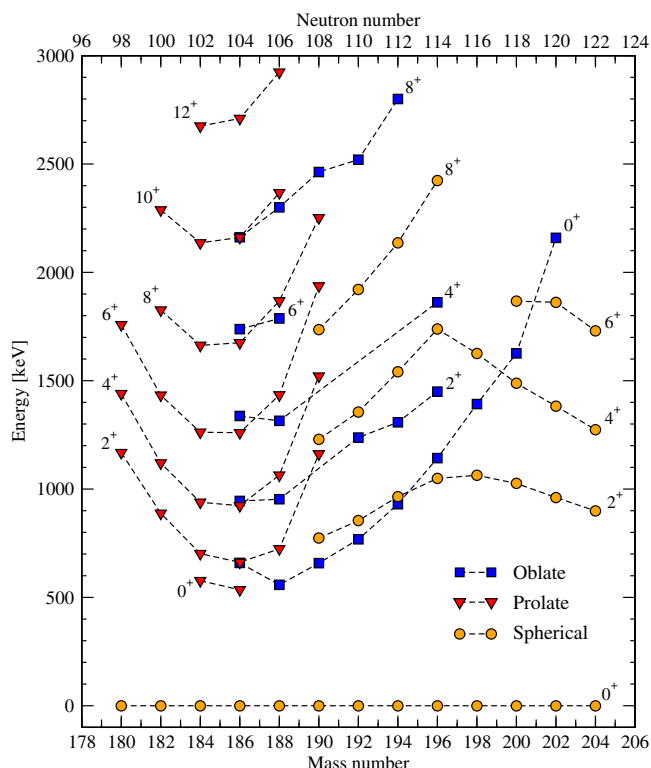


**Fig. 8 Adapted level energy systematics of the neutron-deficient even-mass Pb nuclei.** The different predominant intrinsic configurations have been labelled and connected with dashed lines. Data are from the present work and refs. <sup>4</sup>.

extrapolation from the high-spin members of the prolate band and (iii) reduced  $^{190}\text{Po}$   $\alpha$ -decay widths<sup>5</sup>. The competition between the intruding oblate and prolate minima in the neutron-deficient Pb isotopes is most striking at the  $N=104$  mid-shell. In the light of shape staggering between different isotopes<sup>46</sup> and configuration mixing<sup>45</sup> observed in the region, it is questionable whether the level energy systematics can be used as a valid argument for association of  $0^+$  states with specific shape, particularly when direct measurements of shapes, such as the spectroscopic quadrupole moments, are lacking. Secondly, extrapolating the band-head energy from higher spin members of the yrast band is not straightforward in the presence of configuration mixing, particularly when all states involved in mixing are not known. Finally, there is no firm experimental evidence regarding the shape of the ground state in  $^{190}\text{Po}$  and the existing theoretical predictions are conflicting. Beyond mean-field calculations present the ground state as predominantly oblate<sup>29</sup>, whereas particle-core model calculations suggest predominantly prolate shape<sup>47,48</sup>. While the ground state is a mixture of spherical, oblate and prolate configurations with unknown admixtures, reduced  $\alpha$ -decay widths cannot be unambiguously used as a tool to assign the configuration of the  $0_2^+$  state in  $^{186}\text{Pb}$ . It is noteworthy, that many experimental findings providing supporting arguments for the proposed new assignments, such as lifetime measurements of prolate intruder states in  $^{186}\text{Pb}$ <sup>8,9</sup> and in-beam  $\gamma$ -ray spectroscopy of  $^{186}\text{Pb}$  and  $^{190}\text{Po}$ <sup>17,18,48</sup> nuclei, have been published after ref. <sup>5</sup>.

## Conclusions

The  $N=104$  neutron mid-shell nucleus  $^{186}\text{Pb}$  has been studied in a simultaneous in-beam  $\gamma$ -ray and electron spectroscopy experiment employing the SAGE spectrometer and the recoil-decay tagging technique at the Accelerator Laboratory of the University of

Jyväskylä. The nucleus of interest is unique as it possesses a triplet of  $0^+$  states within 700 keV of the ground state.

The existence of the excited  $0^+$  states has been confirmed and their level energies have been determined with higher precision compared to earlier work through direct observation of the  $0_2^+ \rightarrow 0_1^+$  and  $0_3^+ \rightarrow 0_1^+$   $E0$  transitions. The observation of the  $2_1^+ \rightarrow 0_2^+$  transition allowed the collectivity of the transition feeding the band-head  $0_2^+$  state to be assessed. The  $B(E2; 2_1^+ \rightarrow 0_2^+)$  value obtained suggests the  $0_2^+$  state has a large prolate admixture. To the best of our knowledge, this marks the first observation of a transition feeding an excited predominantly prolate  $0^+$  state in Pb nuclei.

Simultaneous measurement of conversion electrons and  $\gamma$  rays and intensity analysis revealed  $E0$  components in the interband  $2_2^+ \rightarrow 2_1^+$  and  $4_2^+ \rightarrow 4_1^+$  transitions. This allowed for firm assignments of the  $2_2^+$ ,  $4_2^+$ ,  $6_2^+$  and  $8_2^+$  states that form part of the predominantly oblate band.

The two-level mixing calculations performed in the present work indicate that the  $2^+$  and  $4^+$  states are close to pure states with predominant components of  $\sim 90\%$  and  $\sim 96\%$ , respectively.

These findings call for a Coulomb excitation experiment to be performed. The SPEDE spectrometer<sup>49</sup> in conjunction with the Miniball spectrometer<sup>50</sup> with radioactive ion beams from HIE-ISOLDE<sup>51</sup> could provide information on diagonal and transitional matrix elements in  $^{186}\text{Pb}$ . Together with the data obtained in the present work, the monopole strength for interband transitions could be determined. Moreover, the intrinsic configuration of intruder states in this region could be probed in transfer-reaction experiments, e.g., at the ISOLDE Solenoidal Spectrometer<sup>52</sup>. The recoil-shadow method<sup>53</sup> has been proposed<sup>54</sup> to measure the lifetimes of the  $0^+$  states and to extract the monopole strength of the  $E0(0^+ \rightarrow 0^+)$  transitions. In addition, simultaneous in-beam  $\gamma$ -ray and electron spectroscopy could shed light on the configuration assignments of the  $0^+$  band head states in the  $^{188}\text{Pb}$  nucleus.

Results obtained in the present work provide new insight into the nucleus at the heart of triple shape coexistence. It forms the basis for a systematic study of electric monopole transitions in the region and beyond with in-beam spectroscopic methods which have only now become possible.

## Methods

The experiment was performed at the Accelerator Laboratory of the University of Jyväskylä. The use of SAGE+RITU+GREAT<sup>30,55,56</sup> instrumentation, described below, allowed for collection of simultaneous in-beam conversion-electron and  $\gamma$ -ray data employing the recoil-decay tagging method<sup>57,58</sup>. Nuclei of interest were produced via the  $^{106}\text{Pd}(^{83}\text{Kr}, 3n)^{186}\text{Pb}$  reaction with a beam energy of 365 MeV. The  $^{83}\text{Kr}$  beam impinged on a  $1\text{-mg cm}^{-2}$  thick target with intensities varying between 4 and 5 particle nA. During 108 h of beam on target,  $6.34 \times 10^5$   $\alpha$  decays were recorded and correlated with  $^{186}\text{Pb}$  nuclei.

Prompt  $\gamma$  rays and conversion electrons were observed with the SAGE spectrometer. SAGE consisted of 10 EUROAM Phase I and 24 EUROAM Clover-type Compton-suppressed germanium detectors<sup>59</sup> around the target for the detection of  $\gamma$  rays, and an annular segmented silicon detector placed upstream of the target for detection of conversion electrons. Transportation of conversion electrons was made by means of a solenoid coil that was operated with a current of 800 A. The  $\delta$ -electron flux arising from atomic collisions in the target was suppressed by employing a high-voltage barrier at  $-35\text{ kV}$ . The full width at half maximum resolution values of 2.9 keV and 4.5 keV for 261 keV and 662 keV  $\gamma$  rays, respectively, and 11 keV and 14 keV for 173 keV and 447 keV conversion electrons, respectively, were determined from RDT  $\gamma$ -ray and electron singles data.

The RITU gas-filled separator was employed to separate fusion evaporation residues (referred to as recoils in the present work) from the primary beam particles. The GREAT spectrometer, deployed at the focal plane of RITU, was used to identify recoils implanted in the double-sided silicon strip detector (DSSD) based on the deposited energy and characteristic  $\alpha$ -decay energy. The maximum searching time between recoil implantation and the  $^{186}\text{Pb}$   $\alpha$  decay within the same DSSD pixel was 15 s which is equal to approximately three times the half-life of  $^{186}\text{Pb}$  ( $t_{1/2} = 4.83(3)\text{ s}$ )<sup>60</sup>. The shallow implantation depth of recoils allowed for  $\sim 45\%$  of  $\alpha$  particles to escape from the DSSD without full energy deposition. Approximately 19% of the escaped  $\alpha$  particles were detected by the PIN diode box of GREAT installed upstream of the DSSD. The multiwire-proportional counter (MWPC) of GREAT, immediately upstream of the PIN diode box, was used to



measure the energy-loss of the recoils and scattered beam particles in a gas medium and to extract the time-of-flight information between the MWPC and the DSSD.

Data were collected using the fully digital Total Data Readout (TDR) acquisition system<sup>61</sup>. TDR operates without a common hardware trigger and events are time-stamped with a global 100 MHz clock. The GRAIN software package<sup>62</sup> was used for temporal and spatial correlation of events. The final analysis was completed using the ROOT framework<sup>63</sup>.

Due to the long  $\alpha$ -decay searching time, random correlations with  $^{186}\text{Tl}$ ,  $^{187}\text{Tl}$ ,  $^{184}\text{Hg}$  and  $^{186}\text{Hg}$  nuclei gave rise to contaminant events. The false correlation level was  $\sim 6\%$  of all recoils. The contaminant nuclei are well known and their contribution was taken into account in the analysis.

## Data availability

The data obtained in the present work and the corresponding metadata are available from <https://doi.org/10.23729/a6444894-5fe7-4683-a9d5-a8ff1e28208b>.

Received: 6 April 2022; Accepted: 2 August 2022;

Published online: 18 August 2022

## References

- Heyde, K. & Wood, J. L. Shape coexistence in atomic nuclei. *Rev. Mod. Phys.* **83**, 1467–1521 (2011).
- Julin, R., Helariutta, K. & Muikku, M. Intruder states in very neutron-deficient Hg, Pb and Po nuclei. *J. Phys. G: Nucl. Part. Phys.* **27**, R109–R139 (2001).
- Bonn, J., Huber, G., Kluge, H.-J., Kugler, L. & Otten, E. W. Sudden change in the nuclear charge distribution of very light mercury isotopes. *Phys. Lett. B* **38**, 308–311 (1972).
- Julin, R., Grahn, T., Pakarinen, J. & Rahkila, P. In-beam spectroscopic studies of shape coexistence and collectivity in the neutron-deficient  $Z \approx 82$  nuclei. *J. Phys. G: Nucl. Part. Phys.* **43**, 024004 (2016).
- Andreyev, A. N. et al. A triplet of differently shaped spin-zero states in the atomic nucleus  $^{186}\text{Pb}$ . *Nature* **405**, 430–433 (2000).
- Van Duppen, P. et al. Observation of low-lying  $J^\pi = 0^+$  states in the single-closed-shell nuclei  $^{192-198}\text{Pb}$ . *Phys. Rev. Lett.* **52**, 1974–1977 (1984).
- Van Duppen, P., Coenen, E., Deneff, K., Huyse, M. & Wood, J. L. Low-lying  $J^\pi = 0^+$  states in  $^{190,192}\text{Pb}$  populated in the  $\alpha$ -decay of  $^{194,196}\text{Po}$ . *Phys. Lett. B* **154**, 354–357 (1985).
- Grahn, T. et al. Collectivity and configuration mixing in  $^{186,188}\text{Pb}$  and  $^{194}\text{Po}$ . *Phys. Rev. Lett.* **97**, 062501 (2006).
- Grahn, T. et al. Lifetimes of intruder states in  $^{186}\text{Pb}$ ,  $^{188}\text{Pb}$  and  $^{194}\text{Po}$ . *Nucl. Phys. A* **801**, 83–100 (2008).
- Wrzosek-Lipska, K. et al. Electromagnetic properties of low-lying states in neutron-deficient Hg isotopes: Coulomb excitation of  $^{182}\text{Hg}$ ,  $^{184}\text{Hg}$ ,  $^{186}\text{Hg}$  and  $^{188}\text{Hg}$ . *Eur. Phys. J. A* **55**, 130 (2019).
- Gaffney, L. P. et al. Shape coexistence in neutron-deficient Hg isotopes studied via lifetime measurements in  $^{184,186}\text{Hg}$  and two-state mixing calculations. *Phys. Rev. C* **89**, 24307 (2014).
- Dendooven, P. et al. Life time measurements of  $0^+$  intruder states in  $^{190,192,194}\text{Pb}$ . *Phys. Lett. B* **226**, 27–30 (1989).
- De Witte, H. et al. Nuclear charge radii of neutron-deficient lead isotopes beyond  $N = 104$  midshell investigated by in-source laser spectroscopy. *Phys. Rev. Lett.* **98**, 112502 (2007).
- Baxter, A. M. et al. Spectroscopy of  $^{186}\text{Pb}$  with mass identification. *Phys. Rev. C* **48**, R2140–R2143 (1993).
- Heese, J. et al. Evidence for low-lying prolate bands in  $^{188}\text{Pb}$  and  $^{186}\text{Pb}$ . *Phys. Lett. B* **302**, 390–395 (1993).
- Reviol, W. et al. Spectroscopy of  $^{186}\text{Pb}$  and  $^{186}\text{Tl}$  via evaporation residue detection. *Phys. Rev. C* **68**, 054317 (2003).
- Pakarinen, J. et al. Evidence for oblate structure in  $^{186}\text{Pb}$ . *Phys. Rev. C* **72**, 011304 (2005).
- Pakarinen, J. et al. Investigation of nuclear collectivity in the neutron mid-shell nucleus  $^{186}\text{Pb}$ . *Phys. Rev. C* **75**, 014302 (2007).
- May, F. R., Pashkevich, V. V. & Frauendorf, S. A prediction on the shape transitions in very neutron-deficient even-mass isotopes in the lead region. *Phys. Lett. B* **68**, 113–116 (1977).
- Nazarewicz, W. Variety of shapes in the mercury and lead isotopes. *Phys. Lett. B* **305**, 195–201 (1993).
- Tajima, N., Flocard, H., Bonche, P., Dobaczewski, J. & Heenen, P.-H. Diabatic effects in  $^{186}\text{Pb}$ : a generator-coordinate analysis. *Nucl. Phys. A* **551**, 409–433 (1993).
- Chasman, R. R., Egido, J. L. & Robledo, L. M. Persistence of deformed shapes in the neutron-deficient Pb region. *Phys. Lett. B* **513**, 325–329 (2001).
- Duguet, T., Bender, M., Bonche, P. & Heenen, P.-H. Shape coexistence in  $^{186}\text{Pb}$ : beyond-mean-field description by configuration mixing of symmetry restored wave functions. *Phys. Lett. B* **559**, 201–206 (2003).
- Fossion, R., Heyde, K., Thiamova, G. & Van Isacker, P. Intruder bands and configuration mixing in lead isotopes. *Phys. Rev. C* **67**, 024306 (2003).
- Bender, M., Bonche, P., Duguet, T. & Heenen, P.-H. Configuration mixing of angular momentum projected self-consistent mean-field states for neutron-deficient Pb isotopes. *Phys. Rev. C* **69**, 064303 (2004).
- Rodríguez-Guzmán, R. R., Egido, J. L. & Robledo, L. M. Beyond mean field description of shape coexistence in neutron-deficient Pb isotopes. *Phys. Rev. C* **69**, 054319 (2004).
- Egido, J. L., Robledo, L. M. & Rodríguez-Guzmán, R. R. Unveiling the origin of shape coexistence in lead isotopes. *Phys. Rev. Lett.* **93**, 082502 (2004).
- Nomura, K., Rodríguez-Guzmán, R., Robledo, L. M. & Shimizu, N. Shape coexistence in lead isotopes in the interacting boson model with a gogny energy density functional. *Phys. Rev. C* **86**, 034322 (2012).
- Yao, J. M., Bender, M. & Heenen, P.-H. Systematics of low-lying states of even-even nuclei in the neutron-deficient lead region from a beyond-mean-field calculation. *Phys. Rev. C* **87**, 034322 (2013).
- Pakarinen, J. et al. The SAGE spectrometer. *Eur. Phys. J. A* **50**, 53 (2014).
- Eberth, J. & Simpson, J. From Ge(Li) detectors to gamma-ray tracking arrays—50 years of gamma spectroscopy with germanium detectors. *Prog. Part. Nucl. Phys.* **60**, 283–337 (2008).
- Butler, P. A. et al. Electron spectroscopy using a multi-detector array. *Nucl. Instrum. Methods A* **381**, 433–442 (1996).
- Kankaanpää, H. et al. In-beam electron spectrometer used in conjunction with a gas-filled recoil separator. *Nucl. Instrum. Methods A* **534**, 503–510 (2004).
- Kibédi, T., Garnsworthy, A. B. & Wood, J. L. Electric monopole transitions in nuclei. *Prog. Part. Nucl. Phys.* **123**, 103930 (2022).
- Kibédi, T., Burrows, T. W., Trzhaskovskaya, M. B., Davidson, P. M. & Nestor, C. W. Evaluation of theoretical conversion coefficients using BrIcc. *Nucl. Instrum. Methods A* **589**, 202–229 (2008).
- Dracoulis, G. D. et al. Isomer bands,  $E0$  transitions, and mixing due to shape coexistence in  $^{188}\text{Pb}_{106}$ . *Phys. Rev. C* **67**, 051301 (2003).
- Church, E. L., Rose, M. E. & Weneser, J. Electric-monopole directional-correlation experiments. *Phys. Rev.* **109**, 1299–1306 (1958).
- Dowie, J. T. H., Kibédi, T., Eriksen, T. K. & Stuchbery, A. E. Table of electronic factors for  $E0$  electron and electron-positron pair conversion transitions. *Atomic Data Nuclear Data Tables* **131**, 101283 (2020).
- Wood, J. L., Zganjar, E. F., De Coster, C. & Heyde, K. Electric monopole transitions from low energy excitations in nuclei. *Nucl. Phys. A* **651**, 323–368 (1999).
- Hellemans, V., De Baerdemacker, S. & Heyde, K. Configuration mixing in the neutron-deficient  $^{186-196}\text{Pb}$  isotopes. *Phys. Rev. C* **77**, 064324 (2008).
- Zhang, W. Q. et al. First observation of a shape isomer and a low-lying strongly-coupled prolate band in neutron-deficient semi-magic  $^{187}\text{Pb}$ . *Phys. Lett. B* **829**, 137129 (2022).
- Smirnova, N., Heenen, P.-H. & Neyens, G. Self-consistent approach to deformation of intruder states in neutron-deficient Pb and Po. *Phys. Lett. B* **569**, 151–158 (2003).
- Möller, P., Sierk, A. J., Bengtsson, R., Sagawa, H. & Ichikawa, T. Global calculation of nuclear shape isomers. *Phys. Rev. Lett.* **103**, 212501 (2009).
- Van de Vel, K. et al. Fine structure in the  $\alpha$  decay of  $^{188,192}\text{Po}$ . *Phys. Rev. C* **68**, 054311 (2003).
- Van Duppen, P., Huyse, M. & Wood, J. L. Mixing of intruder and normal states in Pb nuclei. *J. Phys. G: Nucl. Part. Phys.* **16**, 441–450 (1990).
- Marsh, B. A. et al. Characterization of the shape-staggering effect in mercury nuclei. *Nat. Phys.* **14**, 1163–1167 (2018).
- Oros, A. M. et al. Shape coexistence in the light Po isotopes. *Nucl. Phys. A* **645**, 107–142 (1999).
- Van de Vel, K. et al. In-beam  $\gamma$ -ray spectroscopy of  $^{190}\text{Po}$ : First observation of a low-lying prolate band in Po isotopes. *Eur. Phys. J. A* **17**, 167–171 (2003).
- Papadakis, P. et al. The SPEDE spectrometer. *Eur. Phys. J. A* **54**, 42 (2018).
- Warr, N. et al. The Miniball spectrometer. *Eur. Phys. J. A* **49**, 40 (2013).
- Kadi, Y. et al. Post-accelerated beams at ISOLDE. *J. Phys. G: Nucl. Part. Phys.* **44**, 084003 (2017).
- Tang, T. L. et al. First exploration of neutron shell structure below lead and beyond  $n = 126$ . *Phys. Rev. Lett.* **124**, 062502 (2020).
- Backe, H. et al. In-beam spectroscopy of low energy conversion electrons with a recoil shadow method — a new possibility for subnanosecond lifetime measurements. *Z. Phys. A* **285**, 159–169 (1978).
- Pakarinen, J. et al. Recoil-shadow electron spectroscopy of low-lying  $0^+$  states in  $^{186}\text{Pb}$  and  $^{194}\text{Po}$ . Proposal to the JYFL-PAC (2006).
- Leino, M. et al. Gas-filled recoil separator for studies of heavy elements. *Nucl. Instrum. Methods B* **99**, 653–656 (1995).
- Page, R. D. et al. The GREAT spectrometer. *Nucl. Instrum. Methods B* **204**, 634–637 (2003).

57. Paul, E. S. et al. In-beam  $\gamma$ -ray spectroscopy above  $^{100}\text{Sn}$  using the new technique of recoil decay tagging. *Phys. Rev. C* **51**, 78–87 (1995).
58. Simon, R. S. et al. Evidence for nuclear shape coexistence in  $^{180}\text{Hg}$ . *Z. Phys. A* **325**, 197–202 (1986).
59. Beck, F. A. EUROBALL: Large gamma ray spectrometers through european collaborations. *Prog. Part. Nucl. Phys.* **28**, 443–461 (1992).
60. Wauters, J. et al. Alpha decay of  $^{186}\text{Pb}$  and  $^{184}\text{Hg}$ : The influence of mixing of  $0^+$  states on  $\alpha$ -decay transition probabilities. *Phys. Rev. C* **50**, 2768–2773 (1994).
61. Lazarus, I. et al. The GREAT triggerless total data readout method. *IEEE Trans. Nucl. Sci.* **48**, 567–569 (2001).
62. Rahkila, P. Grain—a java data analysis system for total data readout. *Nucl. Instrum. Methods A* **595**, 637–642 (2008).
63. Brun, R. & Rademakers, F. ROOT — an object oriented data analysis framework. *Nucl. Instrum. Methods A* **389**, 81–86 (1997).

## Acknowledgements

This work has been supported through the Academy of Finland under the Finnish Centre of Excellence Programme 2012–2017 (Nuclear and Accelerator Based Physics Programme at JYFL), through the Academy Research Fellow funding (contract number 257562) and the European Gamma-Ray Spectroscopy pool. Support from the Science and Technology Facilities Council (UK) and EU 7th framework programme Integrating Activities - Transnational Access, Project No. 262010 (ENSAR) are acknowledged. AH would like to thank the Slovak Research and Development Agency under contract No. APVV-20-0532, and Slovak grant agency VEGA (contract No. 2/0067/21).

## Author contributions

J. Pakarinen, P. Papadakis and D.G.J. prepared the proposal for the experiment. J. Pakarinen, P. Papadakis, J. Sorri, M.S. and D.M.C. set up the instrumentation. K.A., H.B., D.M.C., P.J.D., T.G., P.T.G., J. Henderson, A.H., R.-D.H., J. Hilton, U.J., D.G.J., D.T.J., R.J., S.J., T.K., J.K., G.J.L., M.L., J.L., C.G.M., O.N., R.D.P., J. Pakarinen, P. Papadakis, E.P., J. Partanen, P. Peura, P. Rahkila, J.R., P. Ruotsalainen, M.S., J. Sarén, C.S., J. Sorri, S.S., J.U., A.W. and R.W. monitored the detector, data acquisition and beam systems. J.O., J. Pakarinen, P. Papadakis, R.J. and R.D.P. carried out the data analysis and

interpretation of the data, and J. Pakarinen, J.O., P. Papadakis, R.J., R.D.P., K.A., M.L., P.T.G., R.-D.H., E.P., P. Peura, J. Sorri, J.U. and R.W. prepared the manuscript.

## Competing interests

The authors declare no competing interests.

## Additional information

**Correspondence** and requests for materials should be addressed to Janne Pakarinen.

**Peer review information** *Communications Physics* thanks the anonymous reviewers for their contribution to the peer review of this work.

**Reprints and permission information** is available at <http://www.nature.com/reprints>

**Publisher's note** Springer Nature remains neutral with regard to jurisdictional claims in published maps and institutional affiliations.



**Open Access** This article is licensed under a Creative Commons Attribution 4.0 International License, which permits use, sharing, adaptation, distribution and reproduction in any medium or format, as long as you give appropriate credit to the original author(s) and the source, provide a link to the Creative Commons license, and indicate if changes were made. The images or other third party material in this article are included in the article's Creative Commons license, unless indicated otherwise in a credit line to the material. If material is not included in the article's Creative Commons license and your intended use is not permitted by statutory regulation or exceeds the permitted use, you will need to obtain permission directly from the copyright holder. To view a copy of this license, visit <http://creativecommons.org/licenses/by/4.0/>.

© The Author(s) 2022